PNAS
www.pnas.org

Supplementary Information for

Functional Plasticity and Evolutionary Adaptation of Allosteric Regulation

Megan Leander, Yuchen Yuan, Anthony Meger, Qiang Cui and Srivatsan Raman

Srivatsan Raman
Email: sraman4@wisc.edu

This PDF file includes:

Other supplementary materials for this manuscript include the following:

Movies S1 to S2
Dataset S1 – All_Mutations_Summary.xlsx

www.pnas.org/cgi/doi/10.1073/pnas.2002613117

Supplementary Information Text

Comparison between the computed and experimental SAXS profiles. In a previous study (*1*), Davison and colleagues performed urea-induced protein unfolding experiments on wild-type TetR and mutants. They found that the DNA-binding domain (DBD) of TetR unfolded independently of the ligand-binding domain (LBD). In the ligand-bound state, the unfolding of DBD is coupled to the unfolding of LBD. Therefore, in their unfolding-coupled model, DBD in the apo state is flexible enough to adopt the conformation required for DNA binding. The ligand binding rigidifies DBD to the conformation unfavorable for DNA binding without significantly altering the average structure. Motlagh et al. further assumed that the DBD of TetR is disordered in solution and transitions to a well-folded structure upon ligand or DNA binding (*2*). A recent study, however, contradicts the above model. Hinrichs et. al. performed small angle scattering (SAXS) experiments on the apo and ligand bound TetR. The SAXS profiles showed that both the apo and ligand bound proteins are well-folded in solution and lack major disordered regions (*3*). Therefore, Palm et. al. concluded that no disorder-to-order transition is involved in the induction process.

To evaluate the conformational ensembles sampled in our molecular dynamics simulations, we computed the SAXS profiles based on our MD trajectories and compared the results to the experimental SAXS data. Specifically, we adopted the FOXS method to compute the SAXS profiles for the ligand-bound and apo TetR(B) systems. The profiles of cluster centroids were computed and then reweighted by minimal ensemble search (MES) to best fit the experimental SAXS profiles. The minimized discrepancy χ_2^2 values of the ligand-bound and apo WT TetR(B) systems are 1.13 and 1.10, respectively. As shown in Fig. S10, the computed and experimental profiles match well both in the log(I) plots (Fig. S10 A-B) and in the Kratky plots (Fig. S10 C-D). The MES procedure led to clusters 0 and 7 as the dominant structures for the ligand-bound TetR(B), with a population of 5.5% and 94.5%, respectively. Clusters 6 and 9 are the dominant structures for the apo TetR(B), with a population of 43.0% and 47.0%, respectively. For both the ligand-bound and apo states, the Kratky plots do not decrease to zero for q>0.2 $Å^{-1}$, suggesting considerable structural flexibility in both cases. In short, the good agreement between computed and measured SAXS profiles suggests that the MD simulations adequately capture the solution ensembles; this further confirms that the apo state does not involve any significant unfolding of the DNA binding domain although it features a notable degree of structural flexibility.

Convergence of different properties in MD simulations. As shown in Figs. S11 and S12, the average structure converges rather quickly, reflecting the general structural rigidity of the system. For example, the average structures after 100 ns and 1 μs do not exhibit any major difference at the backbone level (Fig. S12) even for the loop regions, which exhibit higher thermal fluctuations compared to the helices (Fig. S11). The DNA binding domains, despite considerable thermal fluctuations, overlap well for the averaged structures over 100 ns and 1 μs timescales. The general patterns for RMS fluctuations also do not show any major variation beyond 100 ns of sampling, except for several loop regions. These trends apply to all the three TetR variants studied here.

By contrast, properties that reflect correlated motions converge much more slowly. For example, the covariance matrices among the three TetR variants appear rather different after 100 ns (Fig. S13 D-F). Following 1 μs of sampling, however, the differences become substantially smaller (Fig. S13 A-C). The convergence of configurational entropy, which depends on the covariance matrix, is even more difficult, as illustrated by Fig. S13. The overall trend in the computed configurational entropy, which does not clearly distinguish the dead (G102D) and rescuing (G102D/C195F/Q200P) mutants, is similar when only Cα or all heavy (non-hydrogen)

atoms are included in the covariance and entropy calculations. These observations highlight the importance of sampling for probing correlated motions in even relatively rigid systems such as TetR.

Community analysis. In the analysis of protein allostery, it is common to decompose the protein structure into communities, which feature strong intra-community correlations (*4*, *5*). In Fig. S15, we show the results of community analysis for the three TetR variants following 100 ns and 1 ms of sampling. Evidently, the results of community analysis with different amounts of sampling can change considerably, again highlighting the slow convergence of properties that depend on the covariance matrix. Following 1 μs of sampling, the protein structure is divided into several communities and the general pattern does not differ considerably among the three TetR variants studied here, as expected based on the overall similar covariance matrices (Fig. S13). The DNA binding domain is classified as a single community, and it does not contain a significant number of residues in the ligand binding domain. Therefore, the degree of direct coupling between the DNA binding and ligand binding domains is relatively weak, which suggests that allosteric coupling between them occurs through indirect correlations.

Accordingly, we also performed suboptimal path analysis and identified "hub residues" that mediate the "information flow" between these two functional domains. The "hub residues" are sorted in a descending order by the occurrence of each residue in suboptimal paths. The top 50 most-occurred "hub residues" were selected to compare with the "hotspot" residues found experimentally. As shown in Fig. S16, the common set between the two sets of residues contains only a handful of residues, which constitute about 10% percentage of either set. Evidently, the functional significance of "hub residues", at least in TetR based on microsecond simulations, is limited.

Materials and Methods

Centrality scoring. Centrality scores of each residue were calculated using the Network Analysis of Protein Structures (NAPS) server (http://bioinf.iiit.ac.in/NAPS/) (*6*). The unweighted atom pair contact network of the wildtype TetR(B) dimer (PDB ID: 4ac0) was generated using a 0-5 Å threshold. Node centrality was then measured by closeness, or the shortest distance of one position to all others in the network. A two-sample t-test was used to compare the average centrality score of dead hotspots to all other residues in the protein (p=3.2E-06).

Modeling of anhydrotetracycline ligand. The ligand anhydrotetracycline (aTC) was built in Avogadro. To ensure the strong interaction with Mg^{2+}, the hydrogen atom on the O2 atom was removed; this was also consistent with findings from previous electrostatics calculations by Simonson and co-workers. A structure with a total charge of -1 was obtained. The molecule was then optimized in Gaussian using B3LYP/6-31G(d). The optimized structure was uploaded to CHARMM-GUI. Atom types and partial charges were assigned based on the CHARMM General Force Field (CGenFF). The obtained structure and force field parameters were used in all simulations; key protein-ligand/Mg^{2+} contacts observed in the crystal structure were closely monitored during simulations for validating the force field parameters. The chemical structure of the ligand is shown in Scheme S1, and the atom types and partial charges for the ligand are summarized in Table S3.

Molecular dynamics data analysis. CHARMM v41.0 was used to remove the overall translation and rotation and to orient all frames against the crystal structure before any analysis was performed. VMD and Pymol were used to visualize the trajectories. MDAnalysis, numpy, and scikit-learn packages were used for post-processing such as data analysis and plotting.

Correlated motions of protein residues are characterized with the covariance matrix of Cα carbons, which can be represented by either an N x N or 3N x 3N covariance matrix:

$$\mathbf{C} = < (\boldsymbol{q} - < \boldsymbol{q} >)(\boldsymbol{q} - < \boldsymbol{q} >)^T >$$

In the N x N matrix, $\boldsymbol{q} = (\boldsymbol{r}_1; \boldsymbol{r}_2; \ldots; \boldsymbol{r}_N)$ in which $\boldsymbol{r}_i = (x_i, y_i, z_i)$ is the three-dimensional atomic position of the ith atom. In the 3N x 3N matrix, $\boldsymbol{q} = (x_1, y_1, z_1, x_2, y_2, z_2, \ldots, x_N, y_N, z_N)^T$. After normalization, the covariance C_{ij} ranges from -1 to 1. The N x N matrix is plotted in Fig. S13 for illustration, and to help highlight long-range correlated motions, the covariance of contact pairs is set to be 0; the contact probability of Cα pairs is defined as the fraction of frames in which the distance between the pair is less than 10 Å, and only pairs with a probability larger than 0.65 are recognized as contacts.

The 3N x 3N covariance matrix, which reveals more complex correlations, was used in the principal component analysis (PCA) without any filtering. The diagonalization of the 3N x 3N covariance matrix resulted in 3N eigenvalues, which are sorted in the descending order, as are the corresponding 3N eigenvectors.

To compare the difference in free energy landscapes and ensure the consistency in the direction of principal components among the different TetR variants, we merged the three sets of trajectories together and aligned all frames against the crystal structure of the wild type protein. PCA was carried out over the combined trajectory. The projection of each frame onto the eigenvectors resulted in 'Principal Components' (PCs), V_i. The first two PCs, V_1 and V_2, can be used to construct the two-dimensional free energy landscape:

$$\Delta G(V_1, V_2) = -k_B T[ln\rho(V_1, V_2) - ln\rho_{max}],$$

where $\rho(V_1, V_2)$ is an estimate of the joint probability density function obtained from the 2D histogram of the data. ρ_{max} is the maximum density, which is subtracted to ensure $\Delta G = 0$ for the free energy minimum. The 1D free energy landscape can also be constructed as follows:

$$\Delta G(V_i) = -k_B T[ln\rho(V_i) - ln\rho_{max}].$$

The community analysis was carried out by the NetworkView plugin (*7*) in VMD with default setting. The definition of network is the same as that in the paper of Sethi et al (*8*). Each amino acid residue is represented by a node which is connected by edges. The edge weight is $w = -\log|C_{ij}|$, where C_{ij} is the correlation between node i and node j. Here, the N x N covariance matrix was used in which both self-correlations and correlations with the nearest neighboring residues were set to be 0. The path distances between node i and node j are the sum of edge weights along the paths. The shortest distance between node i and node j is found by using the Floyd-Warshall algorithm. The Girvan-Newman algorithm (*9*) was used to partition the communities. Optimal communities can be found by maximizing the modularity value, Q, a measure of the difference in the probability of intra- and inter- community edge (*10*). Suboptimal path analysis was also done in NetworkView with a LengthOffset of 5. The sources are residues interacting with the ligand or Mg^{2+} (residue id 64, 82, 100, 103, 116, 147) and the targets are residues directly involved in DNA-binding (residue id 26, 27, 28, 37, 38, 39, 40, 42, 43, 44, 48). For a given system, the occurrence of a residue is the number of times that the particular residue occurred in suboptimal paths below a threshold (i.e. the shortest distance + LengthOffset).

The quasi-harmonic approximation is commonly assumed in the calculation of configurational entropy of macromolecules. In our case, however, this approximation is unlikely to hold for at least the first two PCs, which exhibit very anharmonic landscape as illustrated in Fig. 4 in the main text. Therefore, the PC1&2 and other PCs were treated differently in the calculation of configurational entropies. In short, we followed the same procedure as in the paper of Andricioaei et al (*11*). except that the PC1&2 were excluded. Then, the contribution of PC1&2 were calculated separately as follows:

$$\mathrm{S} = \mathrm{kln}\frac{\sqrt{2\pi k_B T}}{h}\sum_i e^{-\beta U_i} + \frac{k}{2} + \frac{\sum_i U_i e^{-\beta U_i}}{T\sum_i e^{-\beta U_i}},$$

in which k_B is the Boltzmann constant, T is the absolute temperature, h is the Planck constant, $\beta = 1/k_B T$, and U is the effective potential along PC1 or PC2. The summation index i runs over the number of bins in the corresponding 1D histogram. Since the number of alpha carbons in the wild type and mutants are the same, we can directly compare the difference in configurational entropy between the wild type and each mutant:

$$\mathrm{T}\Delta S = \mathrm{T}S_{mutnat} - TS_{wild\ type}$$

We plot the time evolution of TΔS along the simulated trajectories in Fig. S14A; each point in the curves represents results that include all frames up to that time.

To demonstrate the robustness of the landscape comparison between different TetR variants, the free energy landscapes were also analyzed using the locally scaled diffusion map (LSDmap) (*12, 13*). LSDmap uses a Gaussian kernel to describe the transition probability between two conformations,

$$K_{ij} = \exp\left(-\frac{||\boldsymbol{x}_i - \boldsymbol{x}_j||^2}{2\varepsilon_i\varepsilon_j}\right),$$

where K_{ij} is the transition probability, $||\mathbf{x}_i - \mathbf{x}_j||^2$ is the RMSD between two conformations, ε_i and ε_j are the local scales of the corresponding conformations. We used the procedure proposed in literature (*12*) to determine the local scales. K_{ij} represents the ability of the diffusion of one conformation to the other. This matrix can be easily converted to a Markov matrix, whose eigenvectors represent the diffuse coordinates (DCs). We projected the conformations onto the first two DCs to obtain the corresponding free energy landscapes.

Molecular dynamics simulations for the apo system

To model the apo state of TetR(B), instead of removing the ligand from the ligand-bound structure (PDB ID: 4ac0), we build a model for the apo state with MODELLER (*14*) using the crystal structure of apo TetR(D) (PDB ID: 1bjz) as the structural template. Otherwise, the simulation details are identical to those for the ligand-bound system. The apo simulations are referred to as 4ac0_apo below.

Computed small angle X-ray scattering (SAXS) profiles

The MD trajectories were analyzed with the K-means clustering method implemented in the scikit learn package (*15*). Ten clusters were found for each system and the SAXS profile for each cluster centroid was calculated using FoXS (*16*). The scoring function used by FoXS to evaluate the fitting is defined as,

$$\chi_1 = \sqrt{\frac{1}{M}\sum_1^M \left(\frac{I_{exp}(q_i) - cI_{cal}(q_i)}{\sigma(q_i)}\right)^2},$$

in which *M* is the number of points in the profile, *c* is a scaling parameter, and σ is the experimental standard deviation. The χ_1 was minimized with respect to *c* by the linear least square minimization. A low χ_1 value corresponds to a good fit of computed profile to the experimental profile.

Minimal Ensemble Search (MES) was applied to compute the best fit of the ensemble-averaged SAXS profile to the experimental data (*17*). The scoring function used in MES is as follows:

$$\chi_2^2 = \frac{1}{K-1}\sum_{j=1}^{K}\left[\frac{\mu I_{cal}(q_j) - I_{exp}(q_j)}{\sigma(q_j)}\right]^2,$$

$$\mu = \frac{\sum_{j=1}^{K}\frac{I_{cal}(q_j)I_{exp}(q_j)}{\sigma^2(q_j)}}{\sum_{j=1}^{K}\frac{I_{cal}^2(q_j)}{\sigma^2(q_j)}}.$$

Here, *K* is the number of points in the profiles and $\sigma(q)$ is the experimental standard deviation. With the minimized χ_2^2 value, the optimal weights for different cluster centroids are obtained.

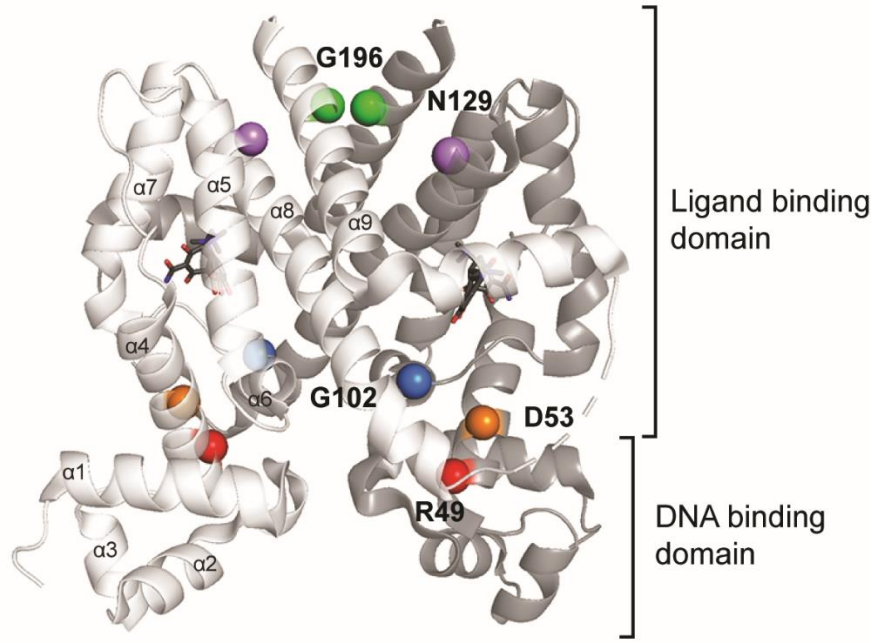

Fig. S1. TetR(B) structure.

Crystal structure of TetR(B) with bound [Minocycline:$Mg]^+$ (PDB ID: 4ac0). Dead variants are labeled as colored spheres on both monomers of the TetR dimer. The ligand and DNA binding domains of the dimer are indicated with alpha helices numbered on one monomer.

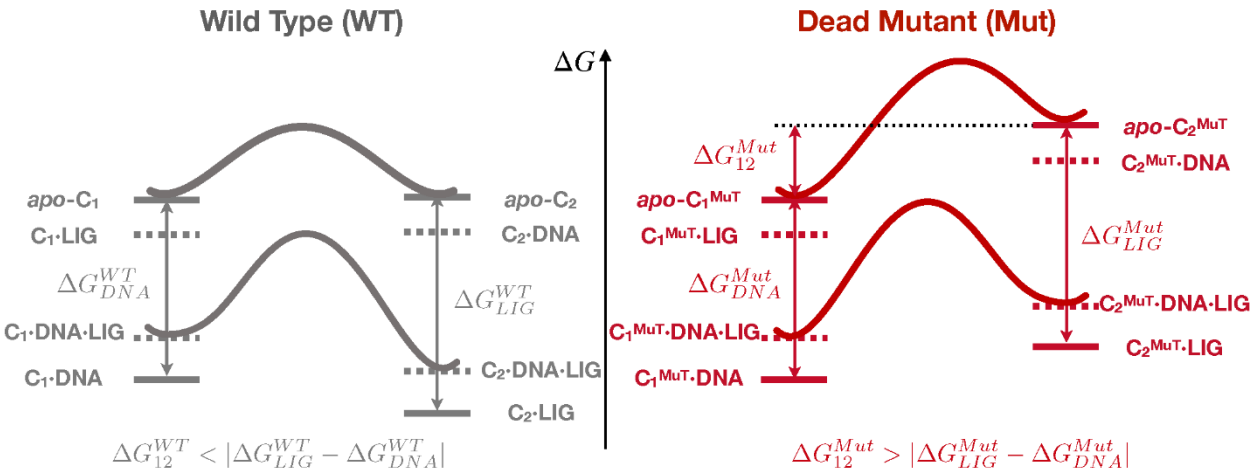

Fig. S2. Comparison of detailed schematic free energy levels and landscapes for the wild type and a dead mutant (Mut) of TetR.

In this simple model, each protein is assumed to have two conformational states (C_1/C_2), which preferably bind to the DNA and the inducer ligand, respectively; for simplicity, we do not separately consider the two ligand/DNA binding domains in each dimeric TetR. Since each protein can adopt four chemical states: apo, the protein-DNA binary complex, the protein-ligand binary complex and the protein-DNA-ligand ternary complex, there are eight stereochemical states for each protein. The effective free energy levels (which in general depend also on the bulk concentrations of ligand and DNA) of these states are indicated with horizontal bars, with the stereochemical states expected to have very low populations shown in dashed bars. The free energy landscape is well defined for systems of the same molecular composition and only two examples for each protein are shown for clarity. In the wildtype protein, the binding affinity of the ligand to apo-C_2 is larger in magnitude than that of the DNA to apo-C_1; assuming that apo-C_1 and apo-C_2 are similar in free energy, this model predicts C_2·ligand as the predominant species (i.e., inducer binding leads to dissociation from the DNA). In a dead mutant, with a simple model, the intrinsic binding affinities of C_1^{Mut} to DNA and C_2^{Mut} to ligand are not perturbed relative to wildtype, but apo-C_2^{Mut} is destabilized relative to apo-C_1^{Mut} by an amount of ΔG_{12}^{Mut}; if ΔG_{12}^{Mut} is larger in magnitude than the differential DNA/ligand binding affinity, $\Delta G_{Lig}^{Mut} - \Delta G_{DNA}^{Mut}$, the model predicts that C_1^{Mut}·DNA is the predominant population even in the presence of the inducer ligand. In other words, ΔG_{12}^{Mut} is the energetic difference that abolishes ligand inducibility by destabilizing the active (C_2^{Mut}) state (or, equivalently, stabilizing the inactive state, C_1^{Mut}). On the other hand, if ΔG_{12}^{Mut} is smaller in magnitude than $\Delta G_{Lig}^{Mut} - \Delta G_{DNA}^{Mut}$, C_2^{Mut}·ligand is still the predominant species; i.e., reduction of ΔG_{12}^{Mut} is likely the mechanism for rescued mutant.

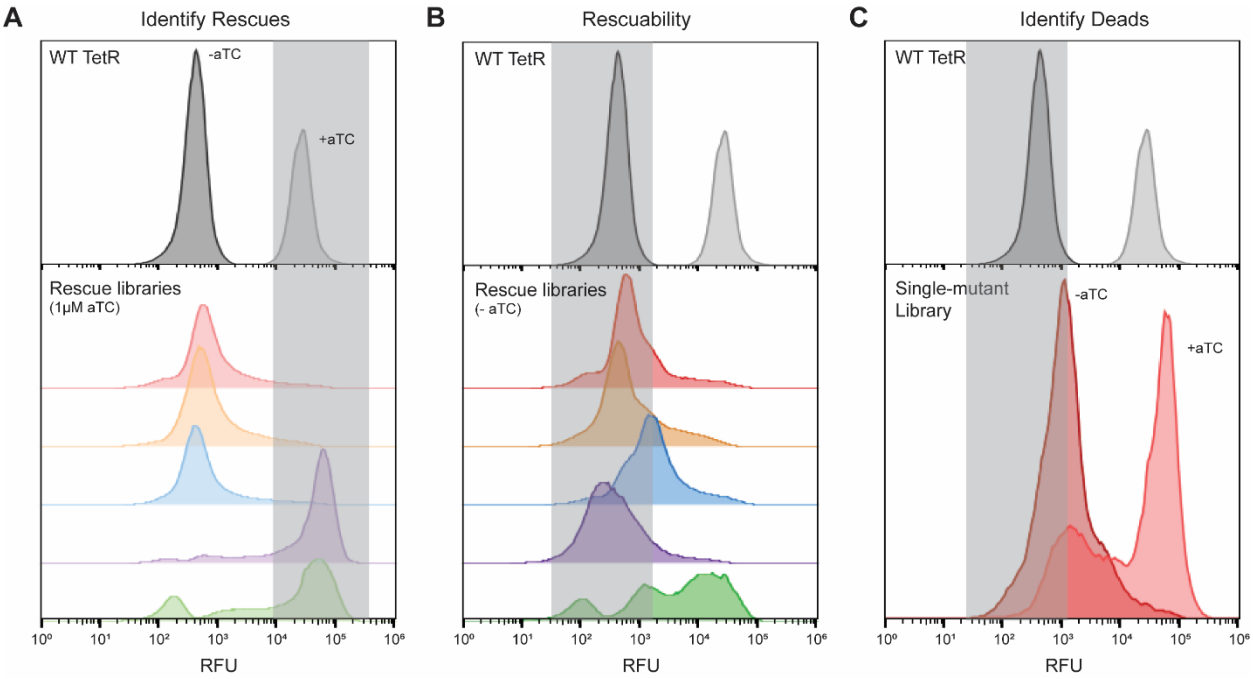

Fig. S3. Sorting schemes for rescuing dead variants and quantifying rescuability. **(A)** To rescue dead variants (Fig. 1) double mutant libraries were induced with 1μM aTC and fluorescent cells sorted (grey bar) and subsequently clonally screened. The distribution of wildtype TetR with induced with aTC was used to select for rescued variants. Libraries are colored as R49A red, D53V orange, G102D blue, N129D purple, and G196D green. **(B)** To quantify rescuability (Fig. 2), non-fluorescent cells in double mutant libraries were sorted (grey bar) in the absence of aTC to select for DNA-bound variants and subsequently clonally screened. The distribution of wildtype TetR without aTC was used to select for DNA-bound variants. **(C)** Nonfluorescent cells in the TetR single-mutant library were sorted (grey bar) in the presence (light red) and absence (dark red) of 1μM aTC and sequenced to identify dead variants.

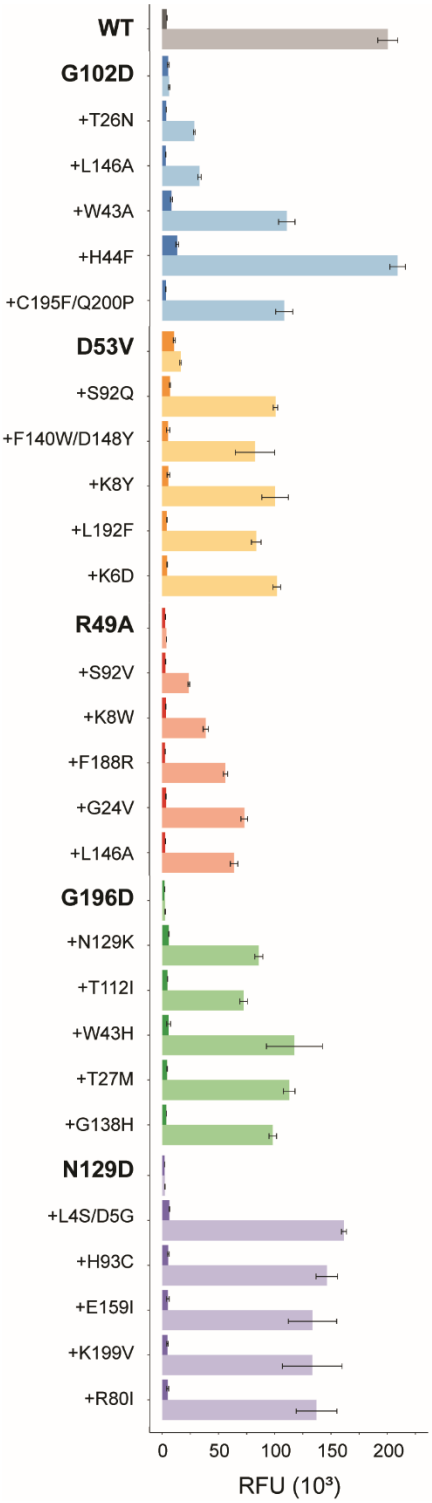

Fig. S4. Mean fluorescence of dead and rescue variants.
Fluorescence of individual TetR variants (mean ± SEM) in the absence (dark bar) and presence (light bar) of 1µM aTC of three biological replicates. Dead variants are shown in bold, and rescued variants are denoted with '+' sign.

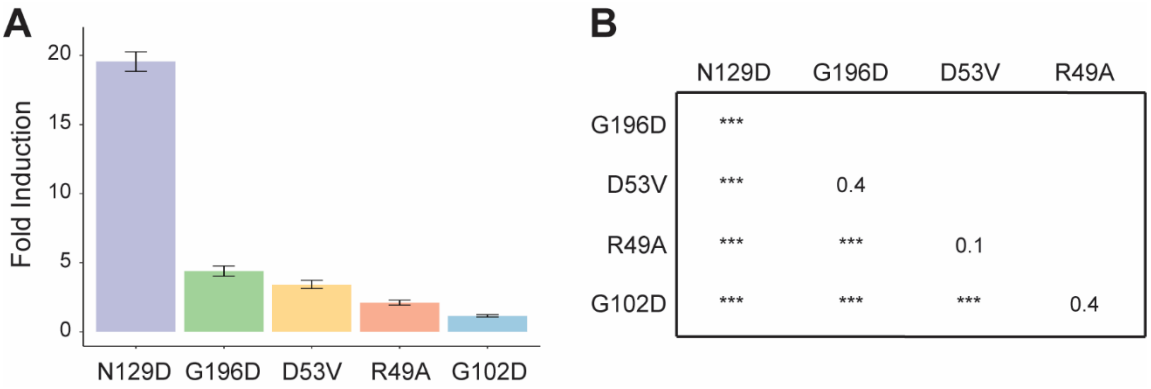

Fig. S5. Ranking of rescuability of each dead variant based on mean fold induction all rescuing variants.

(A) Average fold induction of all screened clones in the presence of 1µM aTC for each dead variant (mean ± SEM). **(B)** Significant differences in fold induction of **(A)** between dead variants are indicated with *p*-values (***$p<0.001$).

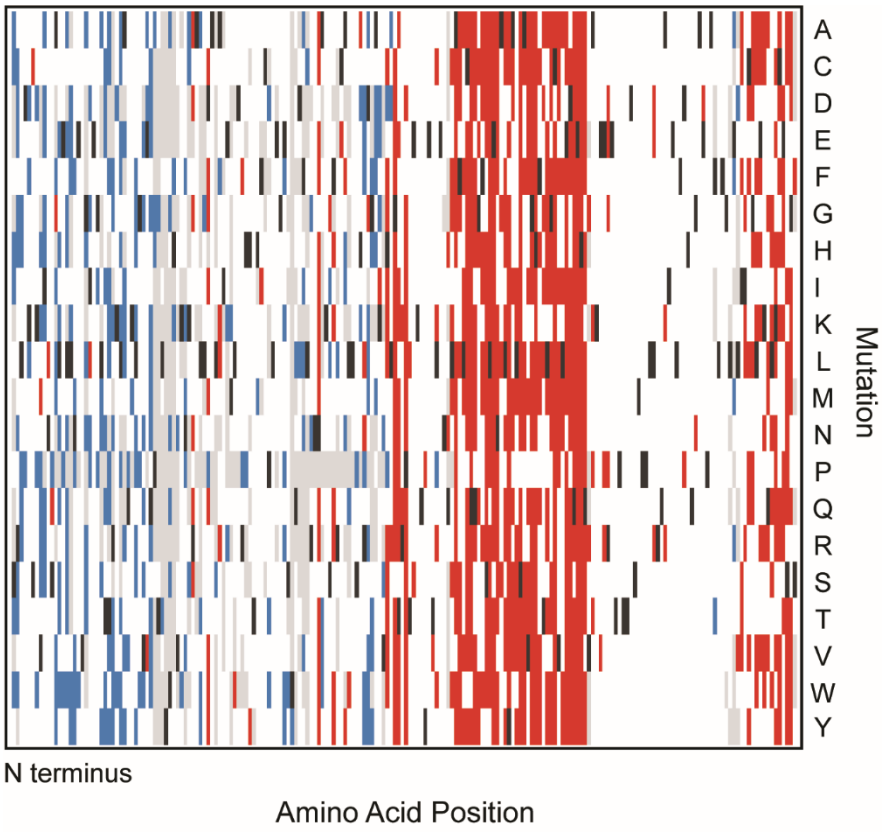

Fig. S6. Dead and broken mutations in TetR.
Dead and broken variants are shown in red and blue, respectively, with the wildtype residue indicated in black and missing data in the library in grey.

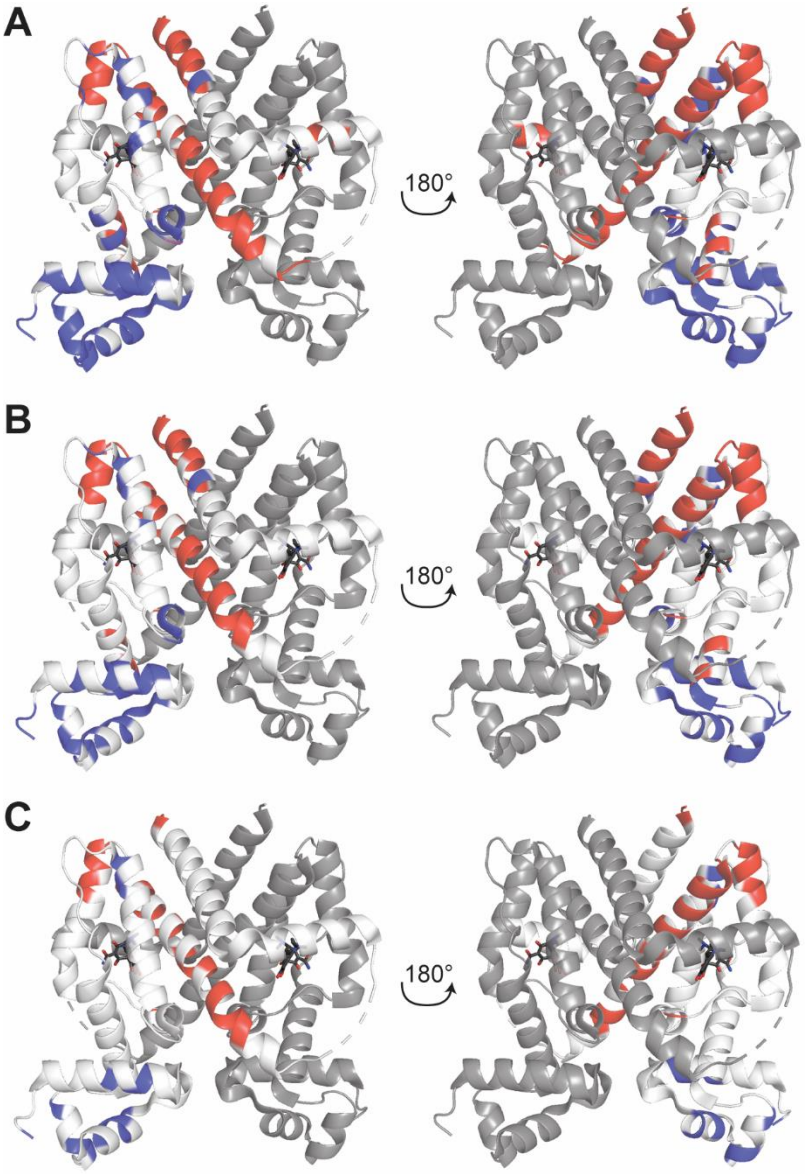

Fig. S7. Threshold for defining of a hotspot does not alter overall regions of importance. Dead (red) and broken (blue) hotspots defined as **(A)** 10%, **(B)** 25%, or **(C)** 50% of all mutations present at that position in the library that inactivate or break the protein are mapped to the structure.

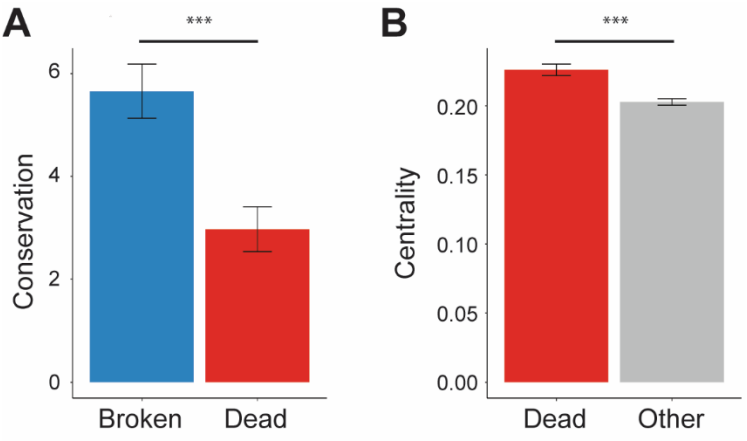

Fig. S8. Significant differences in conservation and centrality of allosteric hotspots. **(A)** Average conservation score of all broken and dead hotspots. **(B)** Average centrality score of dead hotspots compared to all other positions. Data show as mean ± SEM and significant differences indicated (***p<0.001).

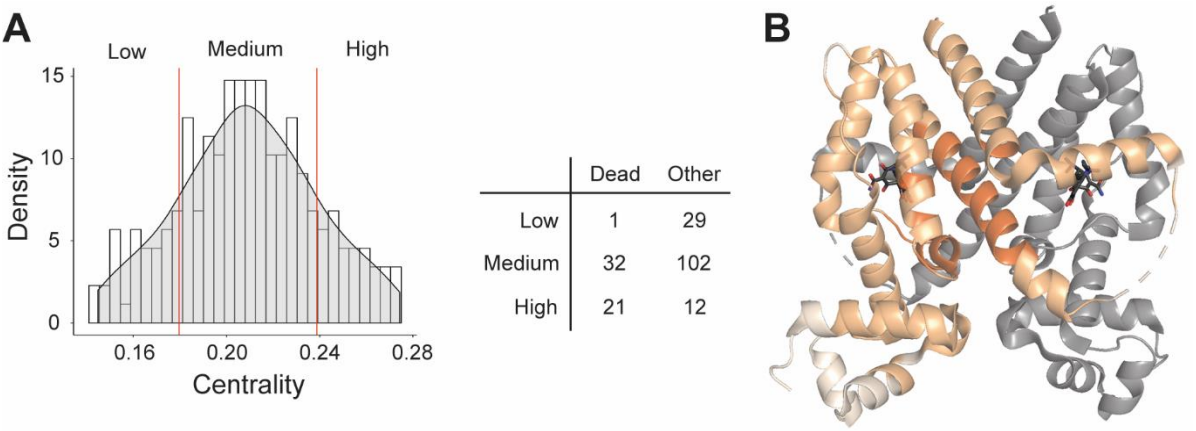

Fig. S9. Hotspots are more likely to occur in positions of high centrality score.
(A) Distribution of centrality scores for all structured TetR positions. Red lines are scores 1σ above and below the mean. Centrality scores are grouped as low, medium, or high based on red lines. The number of hotspots within each group are indicated. **(B)** Positions of low (pale orange), medium (light orange), and high (orange) centrality scores are mapped to TetR.

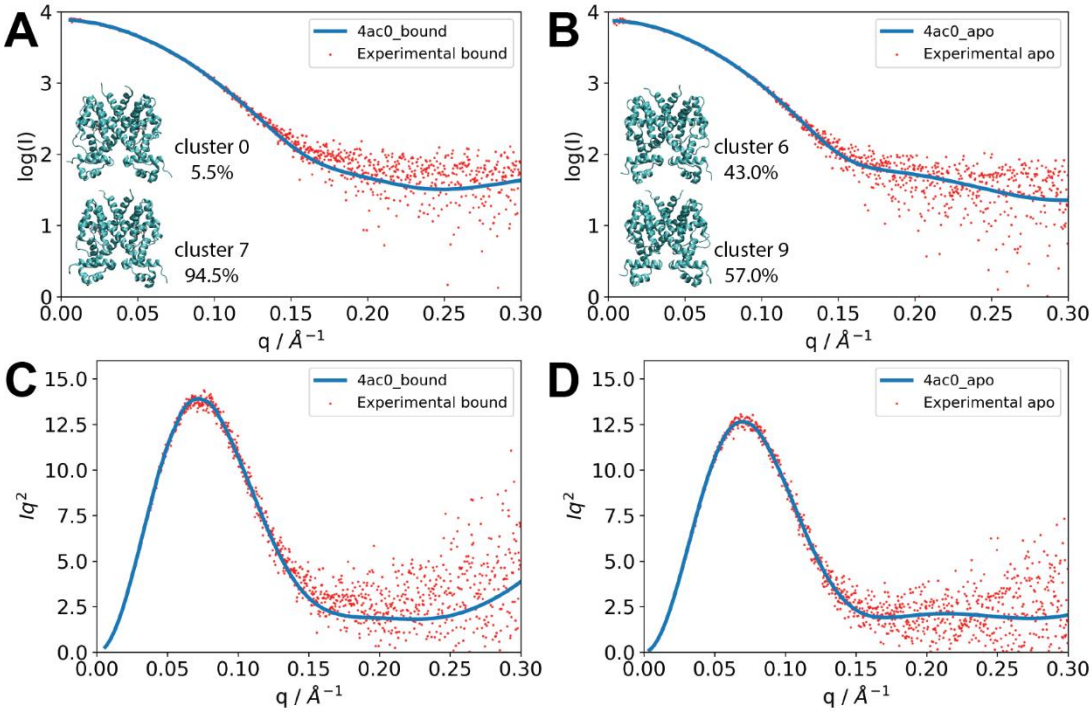

Fig. S10. Comparison of the computed (blue lines) and experimental (red dots) SAXS profiles for ligand-bound and apo TetR systems. For centroid structures obtained from a clustering analysis, SAXS profiles are calculated via FOXS and the populations of the centroids are adjusted through MES to find the best-fit. (**A-B**) The log(I) versus *q* plots for the ligand-bound and apo wild type TetR are shown. The structures with dominant populations found by MES are also shown in each panel. (**C-D**) Kratky plots for the ligand-bound and apo wild type TetR.

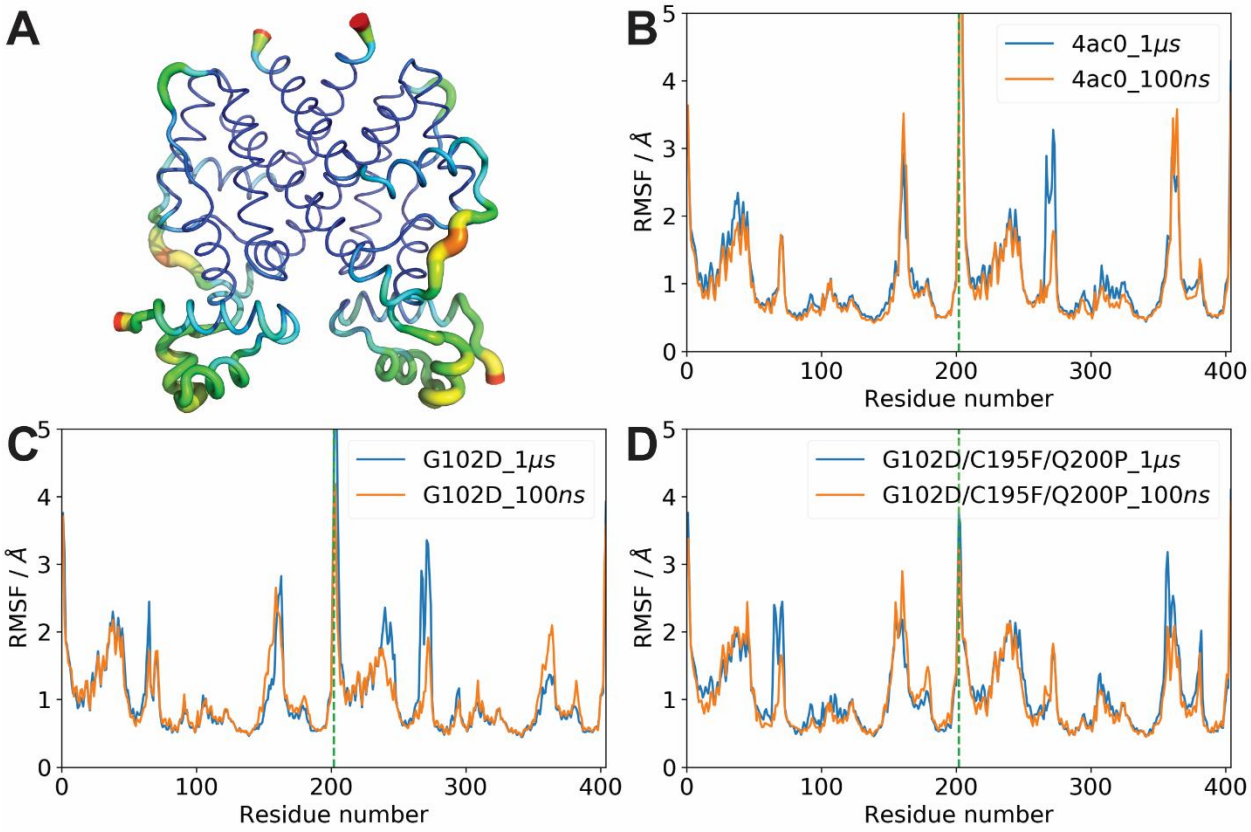

Fig. S11. Structural stability and residue flexibility of TetR in MD simulations.

(**A**) Average structure of the wild type protein with the thickness and color indicating the magnitude of RMSF (root mean square fluctuation). (**B-D**) RMSF of the three systems averaged over 100 ns (orange) and 1 μs (blue).

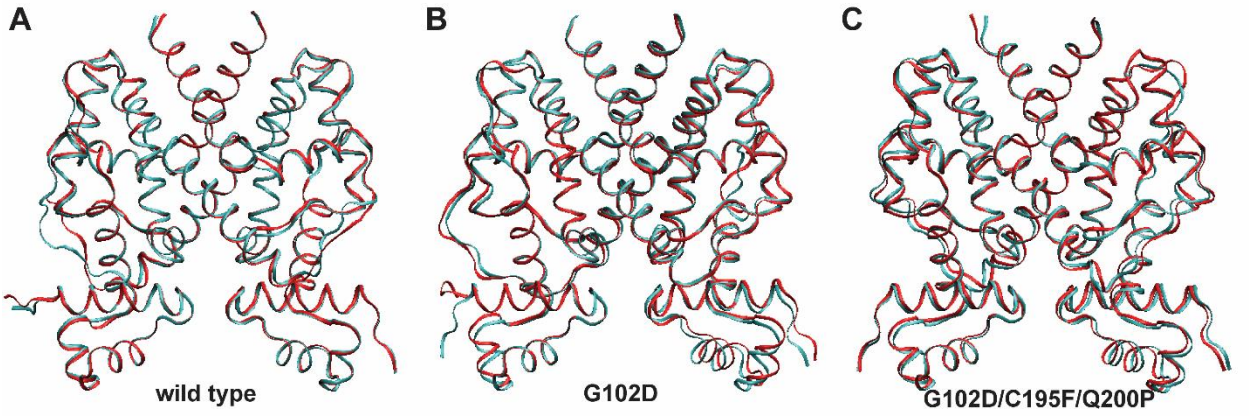

Fig. S12. Convergence and comparison of average structures.
(**A-C**) Overlaid average structure of 100 ns (red) and 1 μs (cyan).

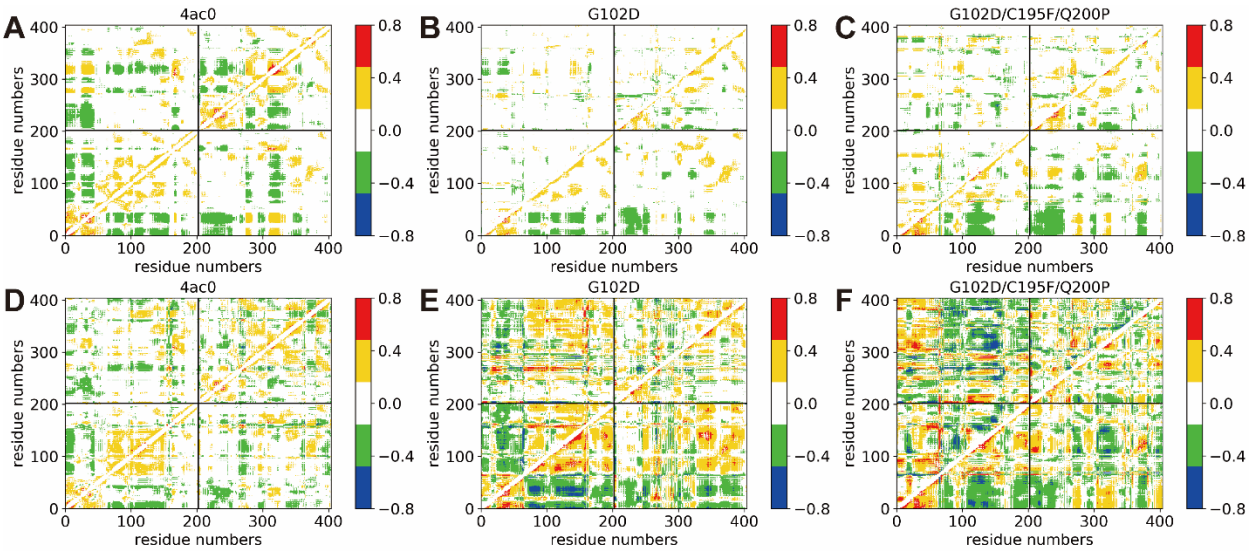

Fig. S13. Covariance of Cα atoms and the convergence of the covariance matrix for wildtype, G102D, and G102D/C195F/Q200P.

(**A-C**) The covariance matrix averaged over the 1 μs trajectories; the upper triangles in (**B**) and (**C**) show the difference in covariance between mutant and wild type proteins. (**D-F**) The covariance matrix averaged over 100 ns trajectories; the upper triangles in (**E**) and (**F**) show the difference in covariance between mutant and wild type proteins.

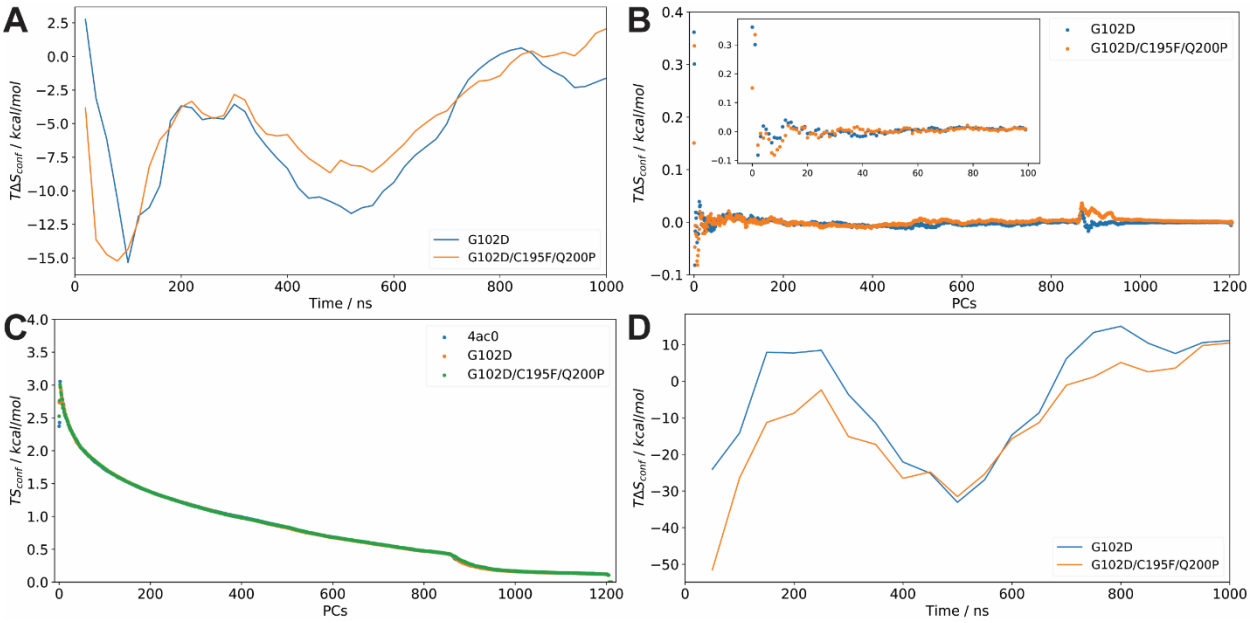

Fig. S14. Conformational entropy converges slowly.

Alpha carbon atoms (**A-C**) in protein were used to calculate the configurational entropy using the modified quasi-harmonic analysis (see text). The temperature, *T*, is 303.15 K. (**A**) $\Delta S = S_{mutant} - S_{wild\ type}$ as a function of simulation time for the two mutants relative to the wild type protein; (**B**) entropic contribution of each mode relative to wild type using the complete (1μs) trajectories; (**C**) entropic contribution of each mode using the complete (1μs) trajectories; (**D**) all heavy (non-hydrogen) atoms were also used to calculate configurational entropy using the same method as above.

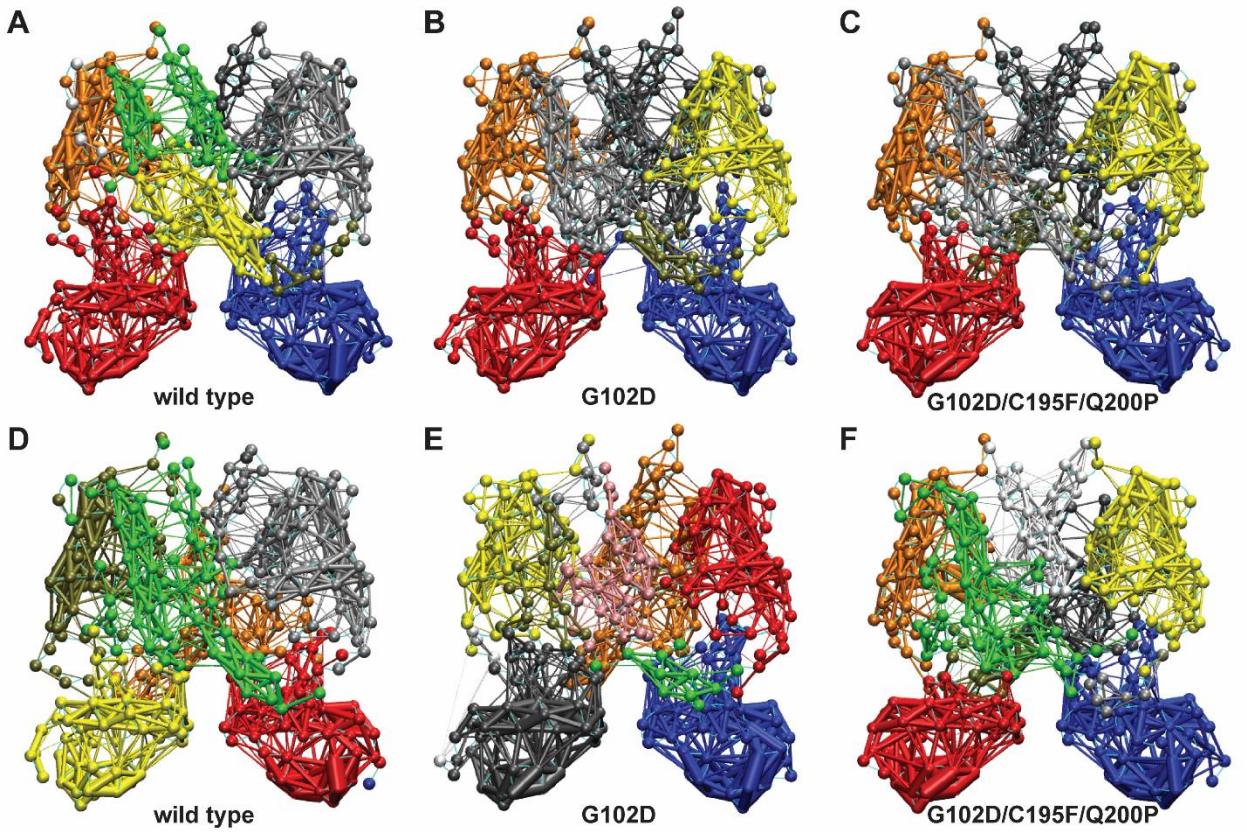

Fig. S15. The partition of structure into communities and convergence of the analysis. (**A-C**) The communities of each system obtained from the 1 μs trajectories. (**D-F**) The communities of each system obtained from the first 100 ns trajectories. Each color represents one community and the choice of color is arbitrary. The solid spheres (nodes) represent alpha carbons and the thickness of lines connecting two nodes represent the magnitude of correlation between two nodes.

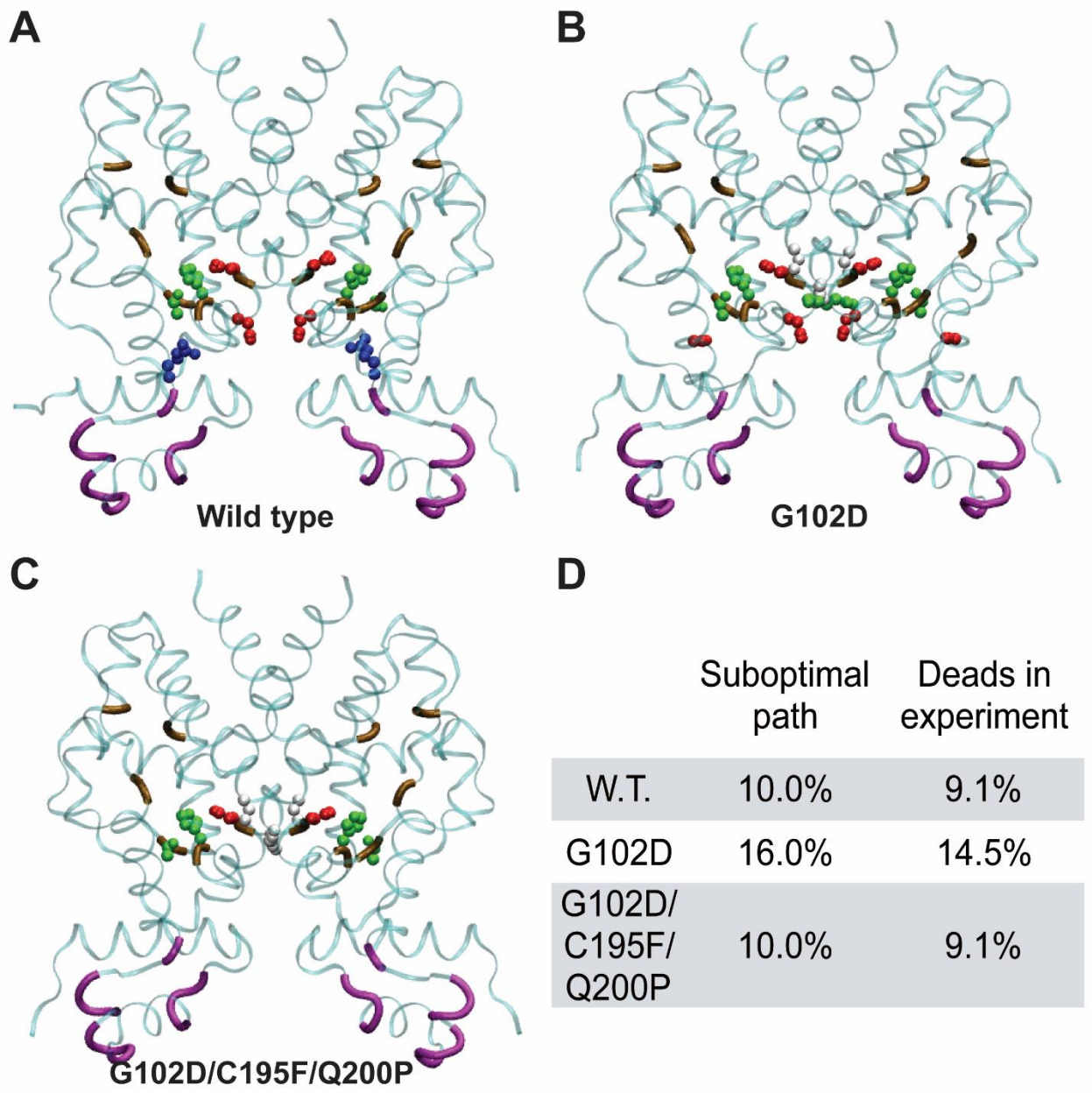

	Suboptimal path	Deads in experiment
W.T.	10.0%	9.1%
G102D	16.0%	14.5%
G102D/ C195F/ Q200P	10.0%	9.1%

Fig. S16. Overlap between 'hotspot' residues identified in experiments and 'hub' residues found in suboptimal path analysis using MD trajectories.

(**A-C**) The protein structures are represented by ribbons and colored by residue types (white for non-polar residues, green for polar residues, blue for negatively-charged residues, and red for positively-charged residues). Residues in ligand-binding domain and residues directly bound to DNA are represented by tubes. The overlapped residues were highlighted as van der Waals spheres in the structures. (**D**) Hub residues are compared with the dead variants in experiments. Hub residues are defined as the top 50 most occurred residues in suboptimal paths for a given TetR variant. Percentages in the second and third columns are the fractions of common residues among the hub residues and the deads in experiments, respectively.

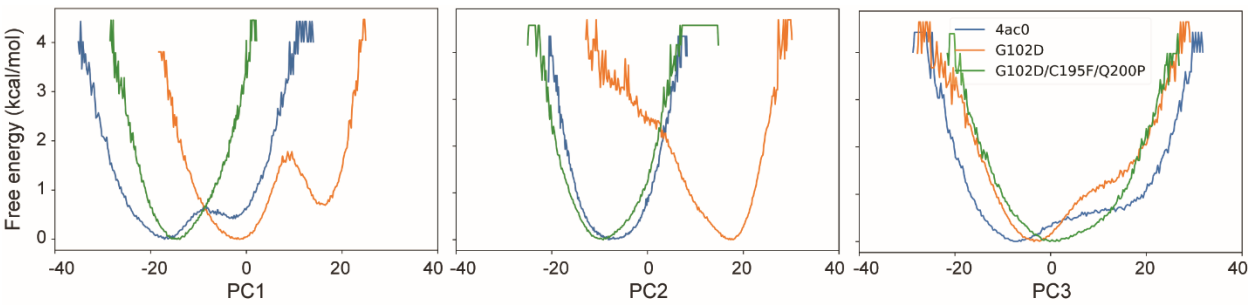

Fig. S17. One-dimensional free energy landscapes along the first three principal components.

Along PC1 and PC2, the landscapes show convergence of the wildtype and rescued variant, but not the dead variant. Beyond PC1 and PC2, the landscapes of all three systems show little difference, indicating that the first two principal components capture the most difference in the free energy landscape.

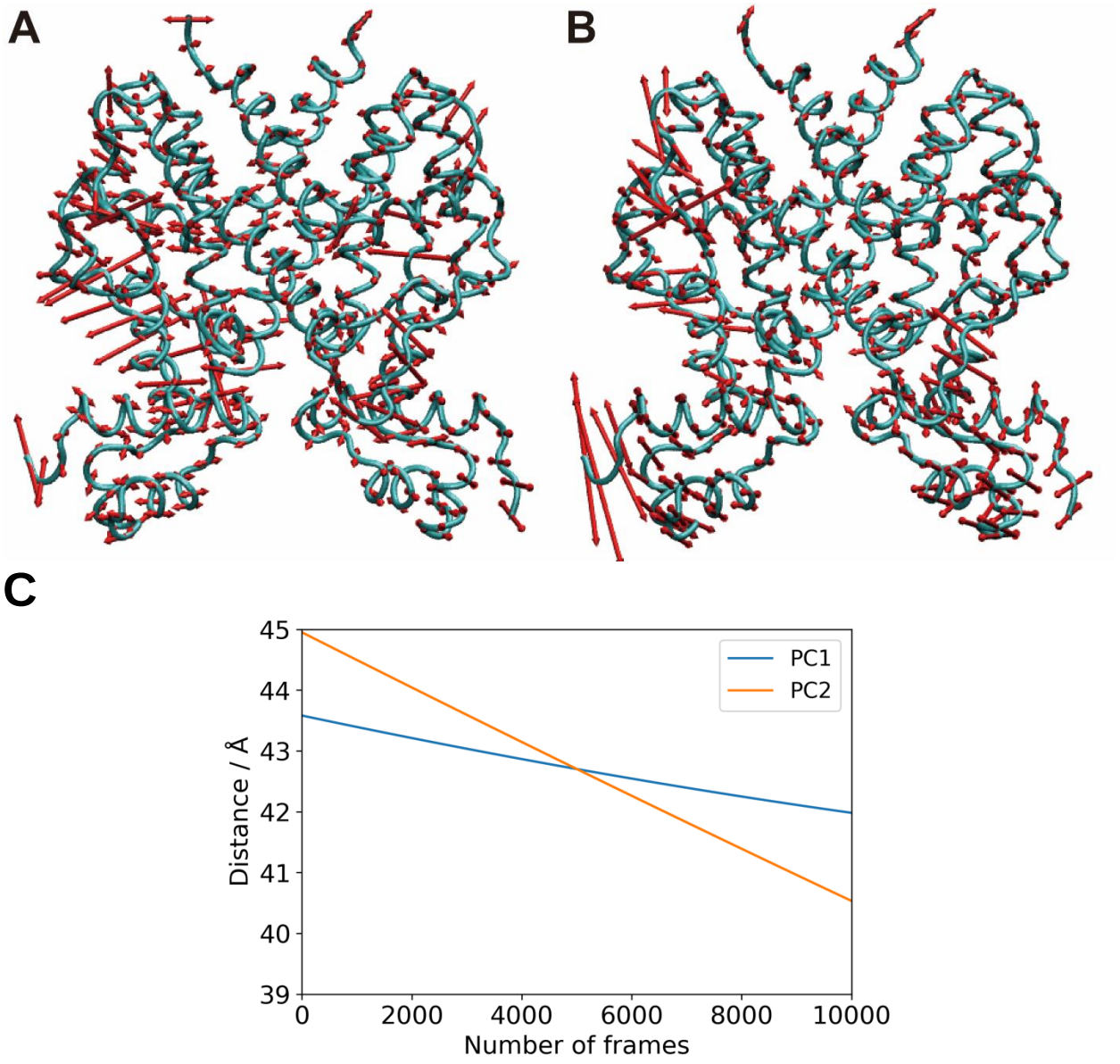

Fig. S18. Directionality and relative magnitude of motions along the first two principal components (also see Movies S1 and S2).

(**A**) First principal component (PC1) mainly represents the motion of loops. (**B**) Second principal component (PC2) represents motions of both loops and DNA-binding domains. The red arrows show the direction of alpha carbons in protein and the length of arrows show the relative magnitude of motion. The pendulum type of motions of the DNA binding domains were proposed to affect the DNA binding affinity and thus activity of TetR. (**C**) As an example, for the evolution of key structural features involved in the first two principal components, the distance between the two α3 helices as a function of displacement along PC1/PC2 is plotted. The plot highlights that both principal components involve relative displacement of the DNA binding domains, a structural transition that has been proposed to modulate the DNA binding activity (*23*, *24*)

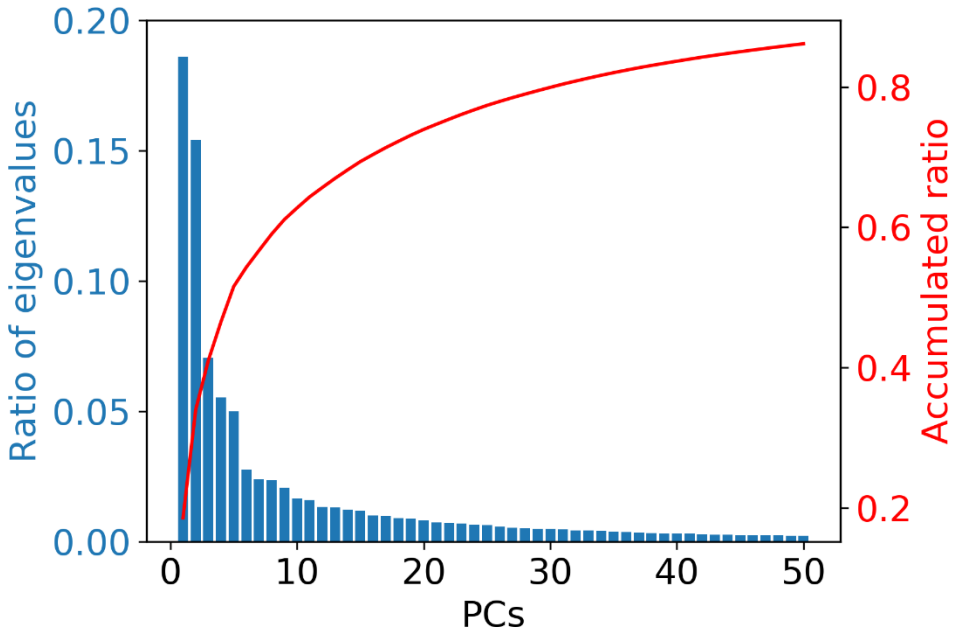

Fig. S19. The first two principal components represent a significant fraction of the motions. The eigenvalues were obtained after performing PCA on the combined trajectories of wild type, G102D, and G102D/C195F/Q200P. Normalization of eigenvalues resulted in the ratios. Although TetR is structurally rather rigid, the first sets of principal components capture a significant fraction of the overall motion; this justifies the use of the first few leading principal components in the free energy landscape analysis discussed in the main text.

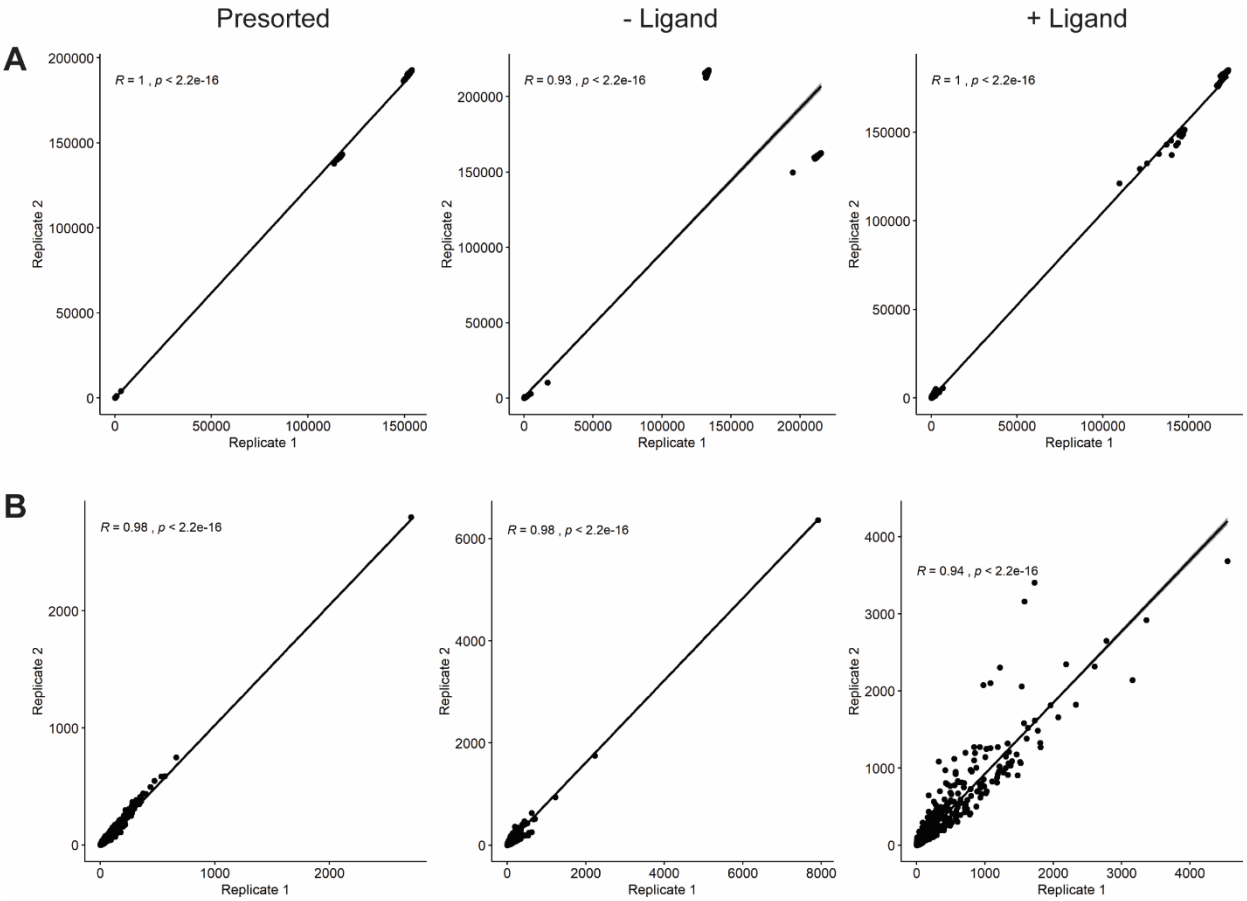

Fig. S20. Strong correlation between replicates in raw and normalized sequencing reads. Sequencing reads from the **(A)** raw and **(B)** normalized data correlate well between replicates for all single mutant libraries: Presorted, uninduced sorted (-Ligand), and induced sorted (+Ligand).

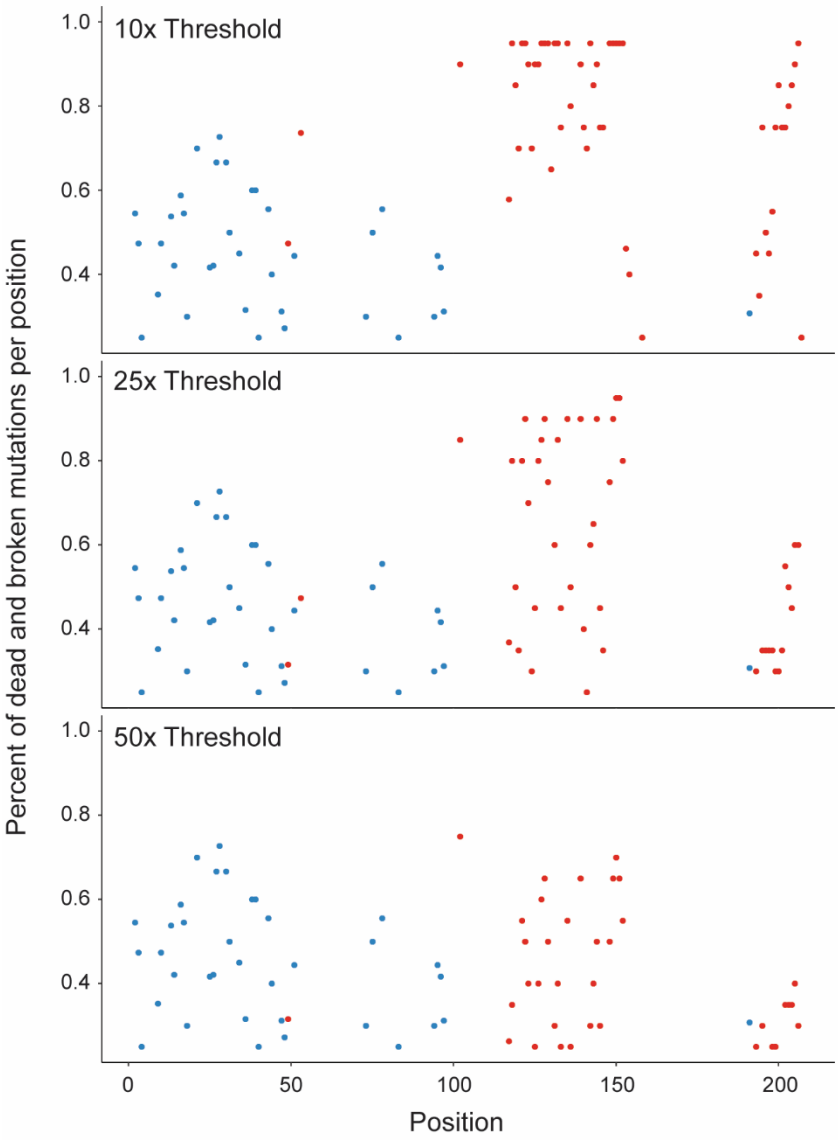

Fig. S21. Dead hotspots change minimally when the read count threshold is altered. The percent of dead (red) and broken (blue) mutations at each position in the protein. Changing the sequencing threshold to 10, 25, or 50 read counts to define a mutation as dead reduces the overall number of dead variants and hotspots, however regions of importance in the protein remain the same.

Dead Variant	Compensatory Mutations
R49A	D5AL, K6HW, G24A, K29IS, E37Y, R87K, H93W, T112P, P184K
D53V	R3V, L4Y, D5A, K6N, K8H, I22C, G24A, L25I, G35DN, R94W, L113C, P184T
G102D	L146A
N129D	L4TY, D5V, K6R, S7P, K8DNW, V9G, A13C, L14N, E19D, I22V, K29Q, L34F, G35F, V36I, E37FH, Q38F, W43K, V45C, K46Y, N47H, L52T, A54FN, A56Q, I57L, E58Y, L60E, H63S, H66Y, F67Y, C68M, P69H, E71L, N81AG, A83GN, T84IT, S85CW, F86CEM, R87Q, C88EHM, A89KY, L91HM, S92M, A97M, K98E, V99F, H100AT, L101H, G102H, R104CSVY, T106V, E107RW, K108S, Q109I, Y110L, E111AIY, T112HNP, L113S, T163L, D164Y, A173E, Q180I, P184V, F188G, I193AC, I184K, C195KTV, G196DIMNPQ, L197AFHPV, E198R, K199CFLQTWY, Q200GHKV, L201GIK, K202ENV, C203DIQSTY, E204ILQST, S205GMVWY, G206CHLMT, S207PQ
G196D	S2CD, D5T, T27M, V36F, E37G, P39S, W43HY, V45FY, A50E, D53V, I57HQ, H63Y, F67CDKLQRSV, C68L, C88R, E107Q, T112IMQRV, F119G, C121P, L131AIVY, S135M, G138HNQ, H139S, L146T, V153R

Table S1. All single-mutant compensatory mutations identified for each dead variant.

TetR Library		Total reads	Good reads	Translated reads	Single mutant reads	Number of variants	Number of variants over 10x threshold	Coverage	Percent wildtype
Replicate 1	Presorted	542436	440570	389212	272093	3759	3442	88%	5.4%
	aTC-	624025	509408	477335	349355	3603	2981		
	aTC+	651400	579330	484690	320675	1912	1213		
Replicate 2	Presorted	654463	525320	468679	336478	3774	3456	88%	5.5%
	aTC-	642040	562346	520758	380410	3611	3005		
	aTC+	682668	597205	496071	336546	2027	1249		

Table S2. Next-generation sequencing statistics of the single-mutant TetR library.

Atom name	Atom type	Partial charge	Atom name	Atom type	Partial charge
O1	OG2D3	-0.48	**O6**	OG311	-0.39
C1	CG2O5	0.442	**C21**	CG2DC1	0.18
C2	CG2R61	-0.331	**C22**	CG2O1	0.567
C3	CG2R61	0.407	**O7**	OG2D1	-0.514
O2	OG312	-0.762	**N2**	NG2S2	-0.714
C4	CG2R61	-0.32	**H1**	HGP1	0.42
C5	CG2R61	0.107	**H2**	HGR61	0.115
O3	OG311	-0.53	**H3**	HGR61	0.115
C6	CG2R61	-0.116	**H4**	HGR61	0.115
C7	CG2R61	-0.113	**H5**	HGA3	0.09
C8	CG2R61	-0.117	**H6**	HGA3	0.09
C9	CG2R61	0.008	**H7**	HGA3	0.09
C10	CG2R61	-0.002	**H8**	HGA2	0.09
C11	CG331	-0.266	**H9**	HGA2	0.09
C12	CG2R61	-0.012	**H10**	HGA1	0.09
C13	CG321	-0.183	**H11**	HGP1	0.42
C14	CG301	0.405	**H12**	HGA1	0.09
C15	CG2O5	0.323	**H13**	HGA3	0.09
O4	OG2D3	-0.471	**H14**	HGA3	0.09
O5	OG311	-0.714	**H15**	HGA3	0.09
C16	CG311	-0.071	**H16**	HGA3	0.09
C17	CG311	0.091	**H17**	HGA3	0.09
N1	NG301	-0.616	**H18**	HGA3	0.09
C18	CG331	-0.099	**H19**	HGP1	0.42
C19	CG331	-0.099	**H20**	HGP1	0.29
C20	CG2D1O	0.035	**H21**	HGP1	0.29

Table S3. The atom name, atom type, and partial charge for the ligand

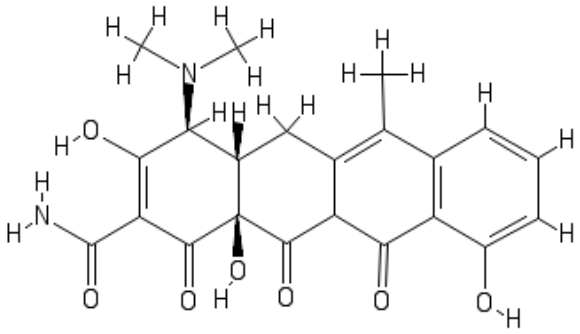

Scheme S1. Chemical structure of anhydrotetracycline

Movie S1. The motion of protein along the first principal component

The motion with the largest amplitude occurred in the loop region, which is consistent with previous analysis. The DNA-binding domain (DBD) resembled the 'pendulum-like' motion, while the patterns of motion are different in two PCs (also see Movie. S2). In PC1, the DBD in two monomers moved toward the same direction.

Movie S2. The motion of protein along the second principal component

The motion with the largest amplitude occurred in the loop region, which is consistent with previous analysis. The DNA-binding domain (DBD) resembled the 'pendulum-like' motion, while the patterns of motion are different in two PCs (also see Movie. S1). In PC2, the DBD in two monomers moved toward the opposite direction.

Dataset S1. Phenotypic summary of all TetR mutations (separate file)

A matrix of all mutations found to be dead (D) or broken (B) indicated at each position in the protein along with the wildtype residue (WT). Blank cells could not be definitively classified as either dead or broken and mutations missing in the library are indicated (-). Positions with 25% or more mutations that inactivate or break the protein were labeled with a Dead or Broken phenotype. The calculated conservation and centrality scores for each position are present.

SI References

1. S. E. Reichheld, Z. Yu, A. R. Davidson, The induction of folding cooperativity by ligand binding drives the allosteric response of tetracycline repressor. *Proc. Natl. Acad. Sci.* **106**, 22263-22268 (2009).
2. H. N. Motlagh, J. O. Wrabl, J. Li, V. J. Hilser, The ensemble nature of allostery. *Nature* **508**, 331-339 (2014).
3. G. J. Palm *et al.*, Thermodynamics, cooperativity and stability of the tetracycline repressor (TetR) upon tetracycline binding. *Biochim. Biophys. Acta* **1868**, 140404 (2020).
4. I. Rivalta, M. M. Sultan, N.-S. Lee, G. A. Manley, J. P. Loria, V. S. Batista, Allosteric pathways in imidazole glycerol phosphate synthase. *Proc. Natl. Acad. Sci. USA* **109**, E1428-E1436 (2012).
5. J. Guo, X. Pang, H.-X. Zhou, Two pathways mediate interdomain allosteric regulation in Pin1. *Structure* **23**, 237-247 (2015).
6. B. Chakrabarty, N. Parekh, NAPS: Network analysis of protein structures. *Nucleic Acids Res.* **44**, W375-W382 (2016).
7. J. Eargle, Z. Luthey-Schulten, NetworkView: 3D display and analysis of protein·RNA interaction networks. *Bioinformatics* **28**, 3000-3001 (2012).
8. A. Sethi, J. Eargle, A. A. Black, Z. Luthey-Schulten, Dynamical networks in tRNA:protein complexes. *Proc. Natl. Acad. Sci. USA* **106**, 6620-6625 (2009).
9. M. Girvan, M. E. J. Newman, Community structure in social and biological networks. *Proc. Natl. Acad. Sci. USA* **99**, 7821-7826 (2002).

10. M. E. J. Newman, Modularity and community structure in networks. *Proc. Natl. Acad. Sci. USA* **103**, 8577-8582 (2006).
11. I. Andricioaei, M. Karplus, On the calculation of entropy from covariance matrices of the atomic fluctuations. *J. chem. Phys.* **115**, 6289-6292 (2001).
12. M. A. Rohrdanz, W. Zheng, M. Maggioni, C. Clementi, Determination of reaction coordinates via locally scaled diffusion map, *J. Chem. Phys*., **134**, 124116 (2011).
13. Y. Zheng, Q. Cui, The histone H3 N-terminal tail: a computational analysis of the free energy landscape and kinetics, *Phys. Chem. Chem. Phys*. **17**, 13689-13698 (2015).
14. B. Webb, A. Sali, Comparative Protein Structure Modeling Using MODELLER. *Curr. Protoc. Bioinform.* **54**, 5.6.1-5.6.37 (2016).
15. F. Pedregosa, A. Gramfort, V. Michel, B. Thirion, O. Grisel, M. Blondel, P. Prettenhofer, R. Weiss, V. Dubourg, J. Vanderplas, A. Passos, D. Cournapeau, M. Brucher, M. Perrot, É. Duchesnay, Scikit-learn: Machine Learning in Python. *J. Mach. Learn. Res.* **12**, 2825-2830 (2011).
16. D. Schneidman-Duhovny, M. Hammel, A. Sali, FoXS: a web server for rapid computation and fitting of SAXS profiles. *Nucleic Acids Res.* **38**, W540-W544 (2010).
17. M. Pelikan, G. L. Hura, M. Hammel, Structure and flexibility within proteins as identified through small angle X-ray scattering. *Gen. Physiol. Biophys.* **28**, 174-189 (2009).